Propagation of seismic-induced electromagnetic waves in a semi-infinite porous medium: A Fourier transform approach

R.Arief Budiman, Aqsha Aqsha, Mehran Gharibi and Robert R. Stewart

ABSTRACT

Numerical simulations of seismic-induced electromagnetic waves in a semi-infinite, saturated porous soil were carried out using COMSOL Multiphysics software. The governing equations used are Maxwell's equations and wave (Navier) equations for the elastic displacements in the solid and fluid phases, and linear constitutive equations. The coupling between seismic and electromagnetic waves defines the seismoelectric effect. The simulations were performed in frequency domain over the range of 0-64 Hz. Fast Fourier transform with a frequency range of 1-32 Hz gave us the time-dependent soil responses. The spectra of energy absorption in the solid and liquid phases produce two identical peaks at 25 and 48 Hz. We attribute these peaks to a resonance effect with a slight dissipation from viscous drag force. The electric field produced was dominated by conduction and we did not observe any large-scale dipole formations. The induced magnetic field on the surface is around 1-10 nT from an excitation surface force peaking at 10 MN.

INTRODUCTION

Seismoelectric effect is a conversion of seismic waves into electric field in a porous medium. In 1993, A large scale field experiment was conducted by Thompson and Gist, who were successful in detecting seismic-to-electromagnetic energy conversion at a depth of 300 m in Texas Gulf Coast (Thompson, 1993). They showed clearly that seismic waves can induce electromagnetic disturbances in saturated sediment in the earth. They produced experimental field data and suggest the feasibility of using electrokinetic coupling for measurements of aquifers, including detection of pollutant migration. The mechanism of the electrokinetic conversion was proposed by Pride (1994). He derived the macroscopic governing equations for the coupled electromagnetic and acoustics of the porous media. The equations have the form of Maxwell's equations coupled to Biot's equations.

Butler and Russel (1996) performed a field experiment at a site near Vancouver and showed a clear seismic electrical response due to a single sledgehammer blow. Their model shows the rapid decay of the converted electroseismic signal with distance. Garambois and Dietrich (2001, 2002) conducted field experiments and recorded the presence of electrical signal and performed numerical simulation based on the microscopic governing equations by Pride. They showed that electromagnetic waves induced by the seismic waves were affected by porosity, permeability, fluid salinity, and fluid viscosity. In a laboratory experiment, Block and Harris (2005) studied the conductivity dependence of seismoelectric waves in fluid-saturated sediments. In their experiment and simulation, they detected electric field generated at the fluid-sediment interface by incident seismic waves. Chen and Mu (2005) also performed experimental studies of seismoelectric effects in fluid-saturated porous media and found that the conversion was sensitive to the oil-saltwater interface.

In this paper, we present numerical results from a full three-dimensional numerical model based on Pride's formulation. The 3D nature of the model is essential for obtaining magnetic field. We simplified the Pride model from nine equations to three equations and perform the simulation in frequency domain. The three coupled equations were for three vector fields: the solid phase displacement, relative displacement of solid-fluid phase and electric field. We used the fast Fourier transform to transform frequency-domain data into time-domain.

GOVERNING EQUATION

We follow the derivation of the seismoelectric model by Pride (1994) to model the propagation of coupled electric and mechanical disturbance in a semi-infinite homogenous porous medium. There are nine coupled different equations describes the interaction between acoustic and electromagnetic waves.

$$\nabla \times \mathbf{E} = i\omega \mathbf{B}, \tag{1}$$

$$\nabla \times \mathbf{H} = -i\omega \mathbf{D} + \mathbf{J}, \tag{2}$$

$$\nabla \cdot \tau_B = -\omega^2 (\rho_B \mathbf{u_s} + \rho_f \mathbf{w}), \tag{3}$$

$$\mathbf{J} = \sigma(\omega)\mathbf{E} + L(\omega)(-\nabla p + \omega^2 \rho_f \mathbf{u_s}) \tag{4}$$

$$-i\omega \mathbf{w} = L(\omega)\mathbf{E} + \frac{k(\omega)}{\eta}\left(-\nabla p + \omega^2 \rho_f \mathbf{u_s}\right), \tag{5}$$

$$\mathbf{D} = \varepsilon_0 \left[\frac{\Phi}{\alpha_\infty}(\kappa_f - \kappa_s) + \kappa_s \right] \mathbf{E}, \tag{6}$$

$$\mathbf{B} = \mu_0 \mathbf{H}, \tag{7}$$

$$\tau_B = \left(K_G \nabla \cdot \mathbf{u_s} + C \nabla \cdot \mathbf{w}\right)\mathbf{I} + G_{fr}(\nabla \mathbf{u_s} + \nabla \mathbf{u_s}^T - \frac{2}{3}\nabla \cdot \mathbf{u_s}\mathbf{I}), \tag{8}$$

$$-p = C \nabla \cdot \mathbf{u_s} + M \nabla \cdot \mathbf{w}, \tag{9}$$

where ω is the angular frequency, H is the magnetic field, B is magnetic flux density, E is the electric field, D is the electric displacement field, J is the current density, ε_0 is the dielectric permittivity of free air, ϕ is porosity, α_∞ is tortuosity, κ_s is the dielectric constant of the solid, κ_f is the dielectric constant of the liquid, μ_0 is the magnetic permeability, L is the coupling coefficient, K_G, C, M, and G_{fr} are elastic constants of the porous media, ρ_f is fluid density, ρ_s is solid density, ρ_B is bulk density, k is the transport coefficient, η is viscosity, u_s is solid displacement, p is fluid pressure, τ_B is the bulk stress tensor and, w is the relative solid-liquid displacement.

These equations describe three three-dimensional vector fields: the solid-phase displacement, the relative displacement between the solid and the liquid phases, and the electric field generated. Auxiliary vector fields include magnetic and electric polarizations can be derived from the fundamental three vector fields. In addition, fluid pressure can be obtained from the divergences of the solid-phase and the solid-liquid displacement fields.

These nine governing equations are Fourier-transformed to produce frequency-dependent equations. They can be reduced into three coupled equations below:

$$\begin{aligned}\nabla\times\nabla\times\mathbf{D} &= \omega^2\varepsilon_0\left[\frac{\Phi}{\alpha_\infty}(\kappa_f-\kappa_s)+\kappa_s\right]\mu_0\mathbf{D}+i\omega\mu_0\sigma\mathbf{D}\\ &+i\omega\varepsilon_0\mu_0 L\left[\frac{\Phi}{\alpha_\infty}(\kappa_f-\kappa_s)+\kappa_s\right]\left(\nabla\{C\nabla\cdot\mathbf{u}_s+M\nabla\cdot\mathbf{w}\}+\omega^2\rho_f\mathbf{u}_s\right),\end{aligned} \tag{10}$$

and

$$-i\omega\mathbf{w}=\frac{L\mathbf{D}}{\varepsilon_0\left[\frac{\Phi}{\alpha_\infty}(\kappa_f-\kappa_s)+\kappa_s\right]}+\frac{k}{\eta}\left(C\nabla(\nabla\cdot\mathbf{u}_s)+M\nabla(\nabla\cdot\mathbf{w})+\omega^2\rho_f\mathbf{u}_s\right), \tag{11}$$

and

$$\begin{aligned}-\omega^2(\rho_B\mathbf{u}_s+\rho_f\mathbf{w}) &= K_G\nabla\cdot(\nabla\cdot\mathbf{u}_s\mathbf{I})+C\nabla\cdot(\nabla\cdot\mathbf{w}\mathbf{I})\\ &+G_{fr}\nabla\cdot(\nabla\mathbf{u}_s+\nabla\mathbf{u}_s^T-\frac{2}{3}\nabla\cdot\mathbf{u}_s\mathbf{I}),\end{aligned} \tag{12}$$

where $\omega = 2\pi f$ is angular frequency (f is frequency), D is electric field, ε_o is permittivity of free air, ϕ is porosity, α_∞ is tortuosity, κ_s is the dielectric constant of the solid, κ_f is the dielectric constant of the liquid, μ_0 is the magnetic permeability, L is the coupling coefficient, K_G, C, M, and G_{fr} are elastic constants of the porous media, ρ_f is fluid density, ρ_s is solid density, ρ_B is bulk density, k is the transport coefficient, η is viscosity, u_s is the solid displacement and, w is the relative solid-liquid displacement. These three equations were implemented in the COMSOL Multiphysics v3.2 to simulate our model. The numerical solutions are obtained for $\boldsymbol{u}_s$, $\boldsymbol{w}$, and $\boldsymbol{E}$, from which we can get other physical quantities, such as pressure and magnetic field.

SIMULATION RESULTS

In our model, a cube of size 200 m x 200 m x 200 m (Figure 1) represents the semi-infinite homogeneous, porous soil, and the governing equations are expressed in the Cartesian coordinate system. The values for the solid-phase parameters, including viscosity (η), dielectric constant (κ_s), and the elastic constants correspond to those of

common rock inside the Earth, while for the fluid phase we use those of water, as listed in Table 1. The elastic waves are launched at the centre of the top surface, having a coordinate (x, y, z) = (0,0,0), by a sharp, normalized Gaussian force distribution, with a peak of 10^7 N/m^2. The full-width at a half maximum for the distribution is 20 m wide. We have verified that the elastic response of the soil remains linear for this force distribution chosen to simulate the explosion effect during seismic survey. The boundary conditions for the top surface (z = 0) are of Neumann type for the solid-liquid relative displacement and the electric field. The boundary conditions for the bottom (z = 200) and side faces of the cube are of Dirichlet type. We performed several numerical tests to ensure that the cube's size is sufficiently large to allow for these Dirichlet conditions.

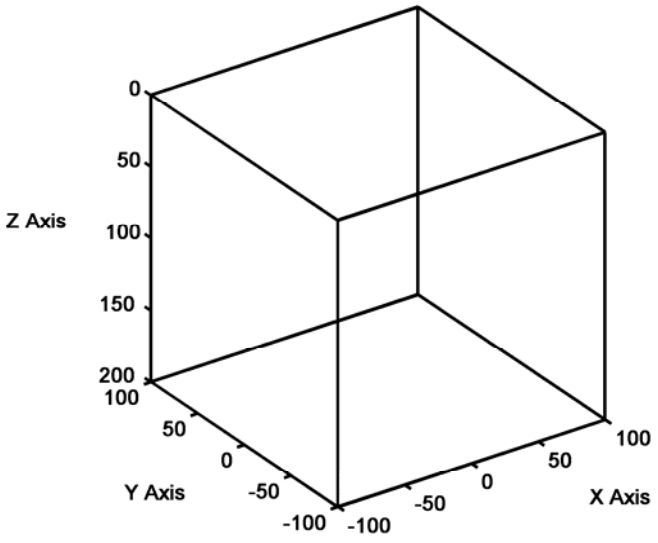

FIG. 1. The cube geometry used for the simulation. The top and bottom surfaces are at z = 0 and z = 200, respectively.

The force distribution is assumed to be of impulse type applied only at t = 0. Its Fourier transform is uniform for all frequencies. When running the simulations at different frequencies, an identical force distribution is therefore used on the top surface. This assumption makes the comparison of the frequency-domain results as a function of frequency relatively straightforward.

Table 1. Parameters of The Semi-Infinite Porous Medium.

Coupling Coefficient (L)	1×10^{-9}
Permittivity of Water (ε)	7.08×10^{-10} F/m
Porosity (ϕ)	0.20
Tortuosity (α_∞)	3

Dielectric Constant of Fluid (κ_f)	2.2×10^{9}
Dielectric Constant of Solid (κ_s)	36×10^{9}
Magnetic Permeability (μ_0)	12.5×10^{-7} H/m
Conductivity (σ)	9.3×10^{-4} S/m
Density of Fluid (ρ_f)	1.0×10^{3} kg/m^3
Density of Solid (ρ_s)	2.7×10^{3} kg/m^3
Constant of Permeability (k)	1.0×10^{-12} cm^2 (1 darcy)
Viscosity (η)	1.0×10^{-3} Pa.s (kg/m.s)
Elastic Constant of Porous Media (G_{fr})	7.0×10^{9} Pa
Frame Bulk Modulus (κ_{fr})	5.0×10^{9} N/m^2
Poisson's Ratio (υ)	0.25
Force at The Surface (F_z)	1.0×10^{7} N/m

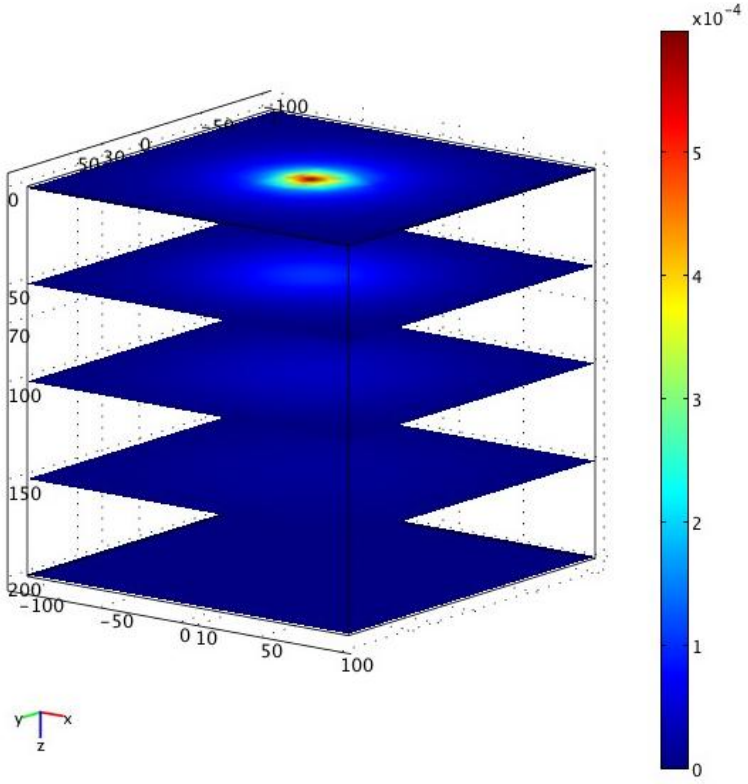

FIG. 2. 3D plot of the *z*-component of the solid displacement vector, u_z. Positive displacement indicates a downward displacement (i.e., toward the positive *z* direction).

Figure 2 shows the *z*-component of the solid displacement vector, u_z, which has a circular symmetry at a frequency of 12 Hz. The maximum u_z on the top surface is 0.6 mm located at the surface's centre. The plot shows a circular symmetric behavior, which is expected, and the displacement magnitude decays to very close to zero at the side surfaces and the bottom surface of the cube. The *z*-component of the displacement at zero frequency should decay like 1/*z* for the vertical direction when the force has a Dirac-δ spatial distribution [Landau, 1995]. The simulation results for u_z at different frequencies show a generally slower decay than the 1/*z* decay behavior, as shown in Figure 3(a). The difference is mainly caused by the force distribution used in our simulation, which is much broader than the Dirac-δ. We have verified in the simulation that for a very sharp force distribution, the decay approaches a 1/*z* behavior.

The *x*-, *y*-, and *z*-components of the solid displacement vector are complex-valued, indicating the influence of viscous effects in the fluid phase. Figure 3(b) shows the imaginary component of the *z*-component for selected frequencies. The magnitude of the imaginary component is almost eight orders of magnitude smaller than the real component shown in Figure 3(a). We observe a drastic change of behavior in u_z around f = 24 Hz. Both the real and imaginary magnitudes jump gradually increase between 16 and 24 Hz. Above 24 Hz, the *z*-component has a negative value, indicating that the elastic displacement of the soil is directed toward the surface. Although this result may seem unphysical since the surface excitation is a compressive force, there is a perfectly valid explanation for it.

a)

b)

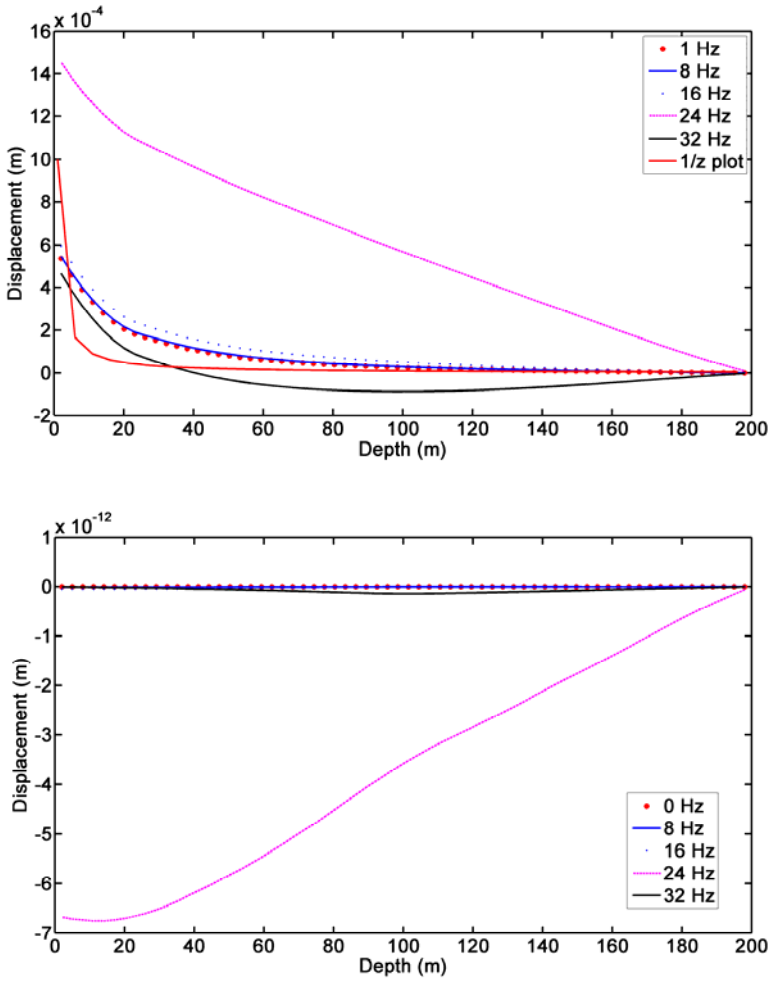

FIG. 3. Solid phase displacement in Z direction in (a) imaginary value and (b) real value for frequency 1-32 Hz.

The frequency-domain elastic response of the material is essentially a time-average with a sinusoidal weighting function as given by the Fourier transform:

$$\mathbf{u}_s(\mathbf{r},\omega) = \int_{-\infty}^{+\infty} \mathbf{u}_s(\mathbf{r},t)\,\exp[i\omega t]\,dt = \int_{-\infty}^{+\infty} \mathbf{u}_s(\mathbf{r},t)\cos\omega t\;dt + i\int_{-\infty}^{+\infty} \mathbf{u}_s(\mathbf{r},t)\sin\omega t\;dt$$

where $i=\sqrt{-1}$. When the angular frequency ω is either too low or too high, the average will be small since the integral of the product of the periodic oscillation of either sine or cosine function and a relatively constant $\mathbf{u}_s(\mathbf{r}, t)$ will yield a value close to zero. When $\mathbf{u}_s(\mathbf{r}, t)$ has a peak, it is possible for $\mathbf{u}_s(\mathbf{r}, \omega)$ to have either a negative or positive peak if the oscillation period matches with the time of occurrence of the peak in $\mathbf{u}_s(\mathbf{r}, t)$ for a particular position $\mathbf{r}$.

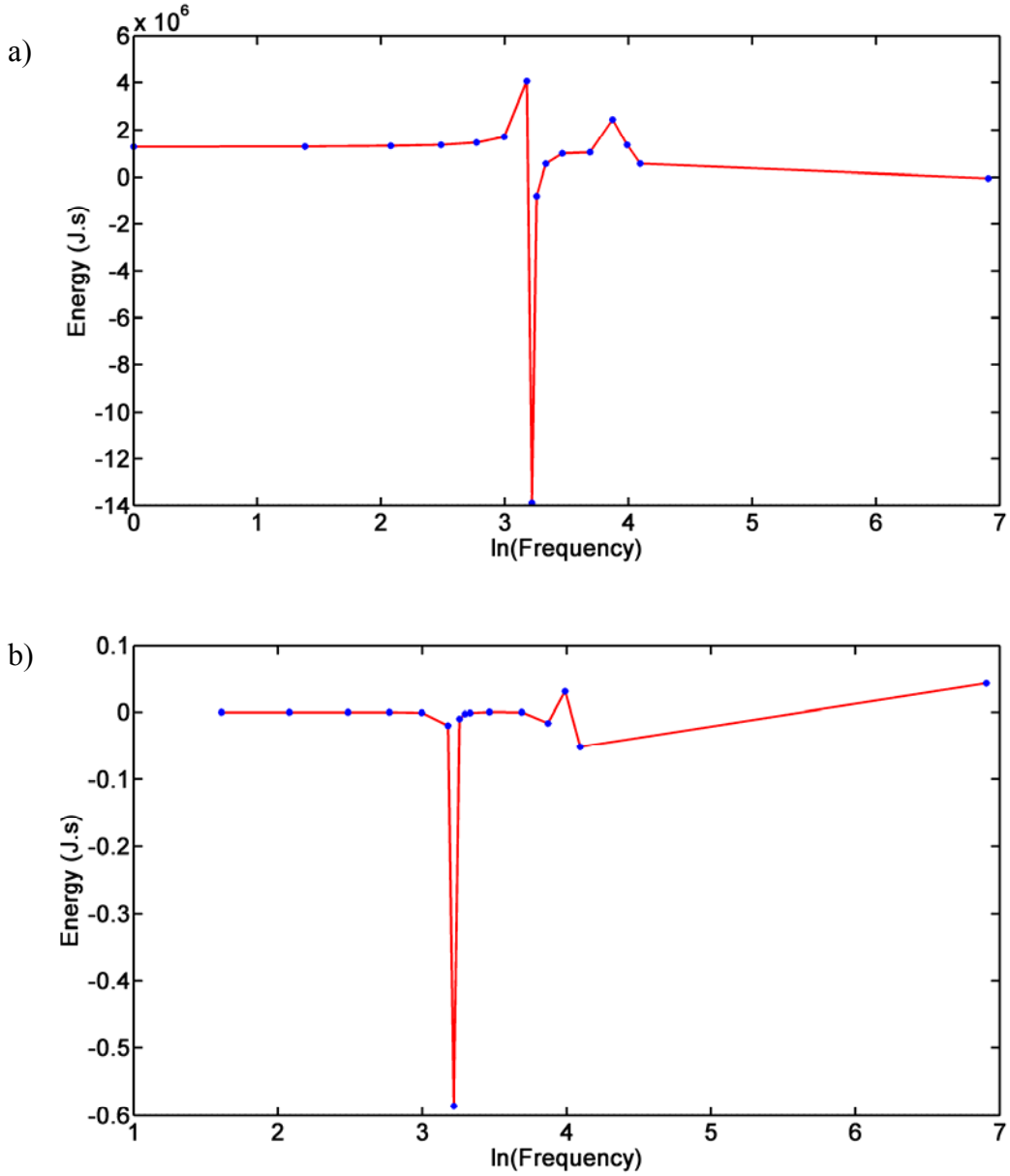

FIG. 4. (a) Real and (b) imaginary components of work done by the force distribution that acts as the external source of seismic and electromagnetic excitations in the simulations.

Figure 4(a) shows the energy W_E injected into the soil as a function of frequency. W_E is the work done to the porous soil by the surface force distribution at a given frequency. This quantity is obtained by summing over the area of the top surface the product of the force distribution and the solid deformation at $z = 0$:

$$W_E(\omega) = A_0 \sum_{(x_i, y_i)} F(x_i, y_i, 0) u_z(x_i, y_i, 0) \quad , \tag{13}$$

where $A_0 = 13.2$ m^2 is the unit area averaged over surface mesh areas. Below 24 Hz, the work done stays relatively constant at about 1.3 MJ·s, but starting from 24 until 55 Hz, the work done changes rapidly. In this frequency range, we observe a positive peak at 24

Hz and a negative peak at 25 Hz. Above 55 Hz, the energy injection decreases with increased frequency. The sudden change of the behavior of the work done at 24-28 Hz we believe is related to a resonance effect. This is confirmed by the presence of a negative peak at 25 Hz imaginary component of the work done shown in Figure 4(b). The imaginary component is due to the imaginary component of u_z.

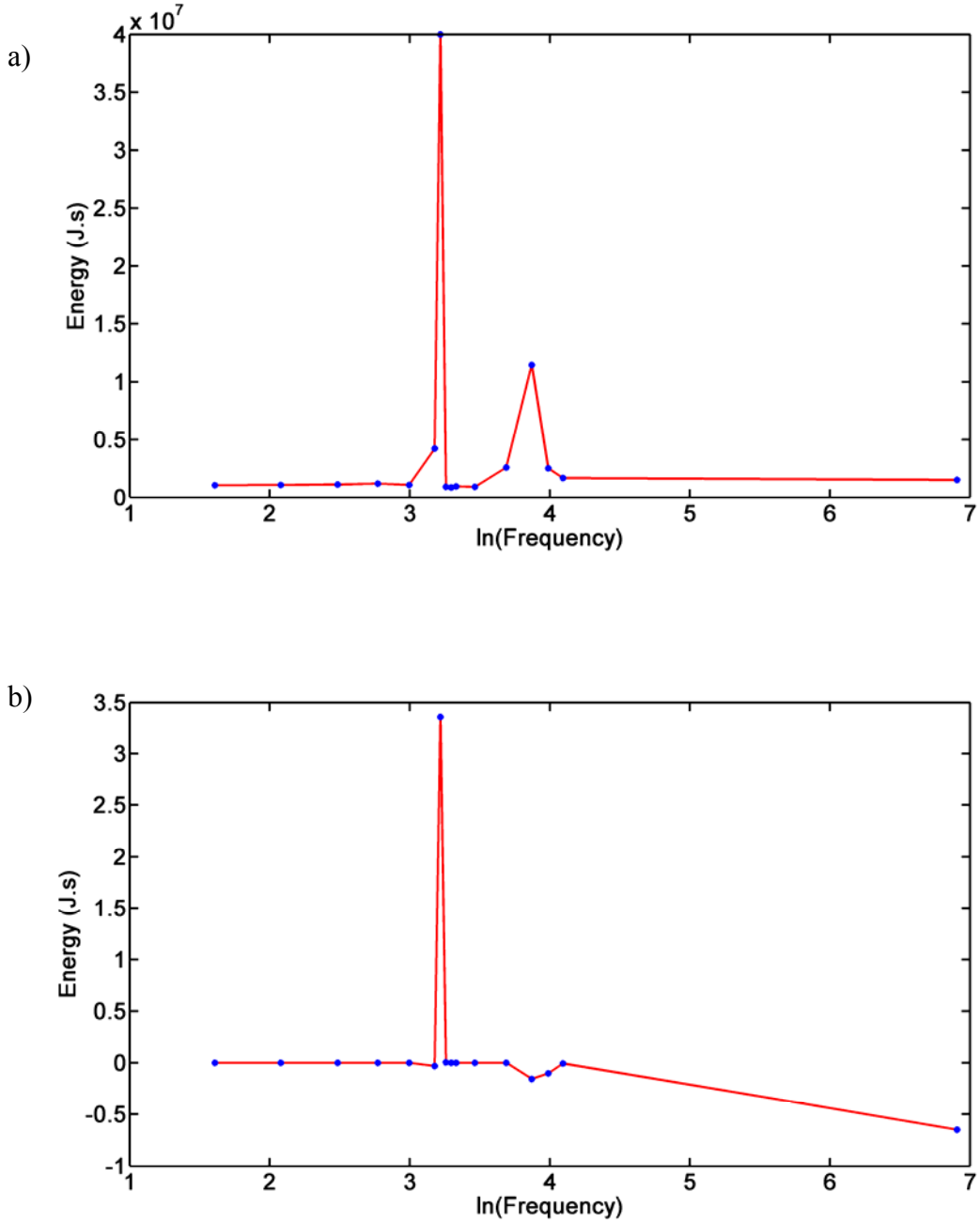

Figure 5. (a) Real and (b) imaginary components of the elastic energy of the solid phase. The real component is the energy absorbed in the solid phase, while the imaginary component is the energy transferred from the liquid phase due to viscosity.

Figure 5(a) is the spectrum of elastic energy stored in the solid phase and confirms the resonance indicated by the work done plot in Fig. 4(a). Figure 5(a) describes the energy absorbed by the solid phase as a function of frequency. The elastic energy density (per unit volume) is calculated using

$$W_S = \frac{E}{1+\nu}\left({u_{ik}}^2 + \frac{\nu}{1-2\nu} {u_{kk}}^2 \right), \tag{14}$$

where E and ν are Young's modulus and Poisson's ratio, respectively, and u_{ik} are the strain tensor of the solid phase (i.e., elastic strains from $\mathbf{u}_s$). The sum of the elastic energy density over the entire volume yields the total elastic energy in the solid phase. The amount of elastic energy in the solid phase does not exceed the energy injected to the soil, except at 25 Hz, where the peak reaches 4×10^7 J·s, higher than the work done peak at 24 Hz in Fig. 4(a). This does not violate the energy conservation, however, since the total elastic energy (summed over the frequency spectrum) in the solid phase is lower than the total energy injected by the force distribution. The 25-Hz peak is within the 24-25 Hz range in Fig. 4(a) where the value changes rapidly from positive to negative. Figure 5(a) shows another smaller, broader absorption peak at 48 Hz, which coincides with the peak at the same location in Fig. 4(a). The imaginary component of the elastic energy in the solid phase, shown in Fig. 5(b), is negligible compared to the real component.

The governing equations for the seismic-induced electromagnetic wave propagation have only fluid viscosity as the dissipation term. The energy stored in the fluid can be estimated by the Biot's model of elastic displacements in a porous medium:

$$W_F = -C\zeta + \frac{1}{2} M \zeta^2, \tag{15}$$

(15)

where C and M are material constants for the fluid phase, and $\zeta = \phi \nabla \cdot (\mathbf{u}_s - \mathbf{u}_f)$ for a given porosity ϕ. The real component of the fluid energy exhibits a positive peak at 25 Hz, as shown in Figure 6(a). The location of the positive peak coincides with the peak in the elastic energy of the solid phase in Fig. 5(a). In fact, the general shape of the fluid-phase energy is almost identical to the solid-phase energy. The magnitude of the fluid-phase energy is eight orders of magnitude smaller than that of the solid. This aspect is rather puzzling: Why does the fluid absorb much less energy than the solid despite the fact that its porosity is 0.2? One fluidic aspect neglected in the calculation of fluid energy is the energy stored as fluid pressure. The Biot formulation, however, neglects the fluid's volume change due to elastic displacement, which gives rise to pressure. The fluid-phase energy in the Biot model only includes the relative displacement between the solid and the fluid phases. The peak in Fig. 6(b) indicates an energy absorption by the fluid phase, which is also reflected in the solid phase.

The coincidence between the fluid and solid energy spectra suggests that both phases move in unison; their relative displacement is very small. The amount of energy absorbed by the liquid is very small compared to the magnitude of the work done (energy input) to the system due to reasons above. However, the resonant frequency (25 Hz) is the same in

both liquid and solid phases. The amount of energy dissipated by the liquid, as given by the imaginary component of the fluid energy, is negligible as graphed in Figure 6(b).

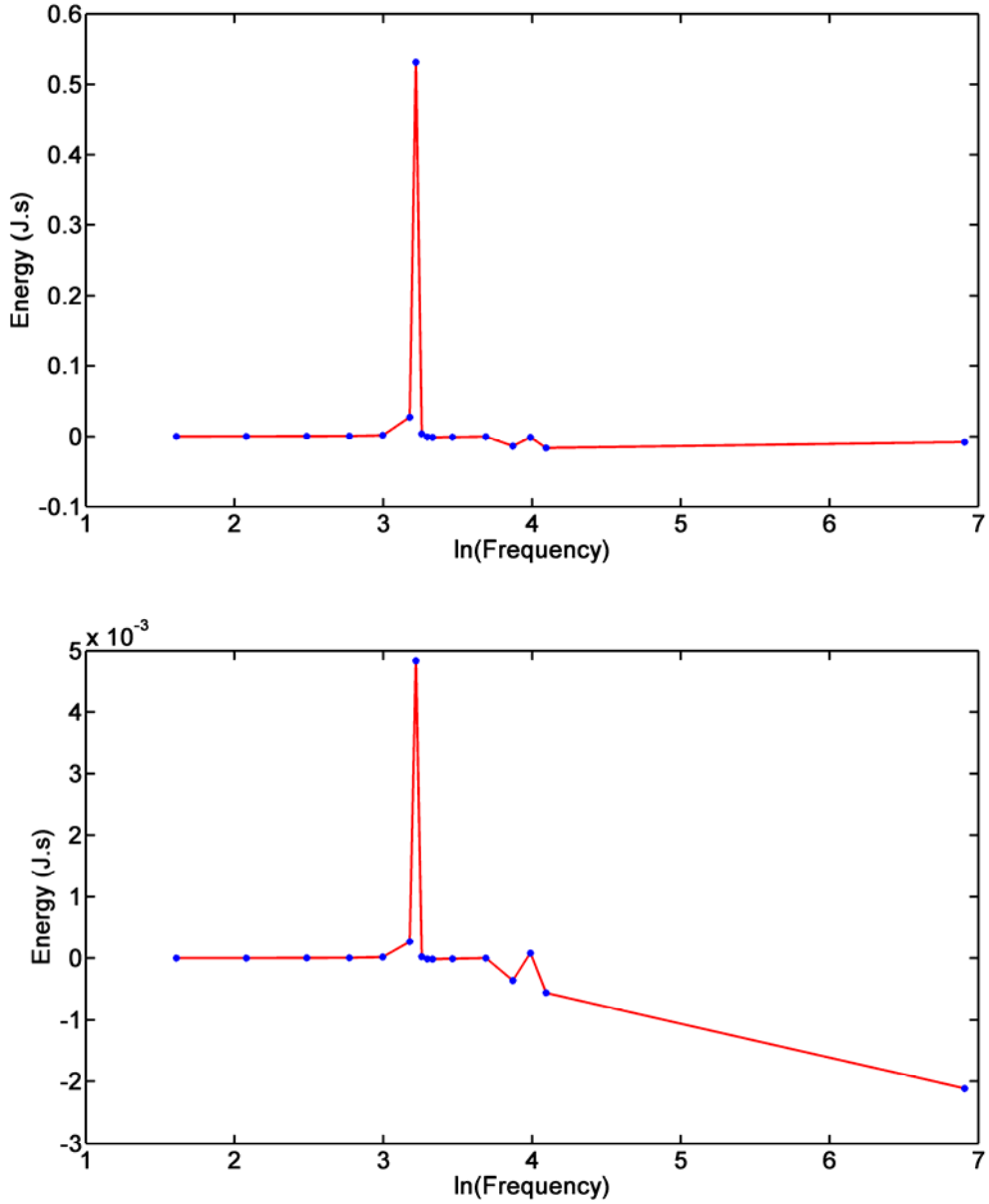

FIG. 6. (a) Real and (b) imaginary components of the energy of the fluid phase.

To understand the resonance effect, we offer an analogy with the classical Lorentz dipole model that explains complex-valued dielectric function, i.e., refractive index. This model is appropriate for describing optical refraction and absorption in dilute dielectric materials, where the absorbing agent is a microscopic electrical dipole. This dipole behaves like a mechanical spring; it does not dissipate energy. The two atoms (or molecules) that make up the dipole have masses. The energy dissipation is provided by energy loss due to collisions and other microscopic effects, which can be represented by a mechanical damper. The spring-mass-damper system with a sinusoidal external excitation,

when analyzed in frequency domain, produces the complex-valued dielectric function. The real part corresponds to the refractive index which has zero value exactly at the frequency where the absorption (resonance) peak occurs. The shape of the real component has the shape of the derivative of a Lorentzian function with respect to the frequency, while the shape of the imaginary component is given by the Lorentzian. The shapes of these components resemble those around the 24 Hz peak shown in Figure 4.

The elastic wave equation coupled with the fluid viscous motion describes coupled nearest-neighbor springs–instead of an isolated spring-mass-damper system–in the governing equations, as evident in equations (5) and (9), where the force is proportional to the gradient of the divergence of the solid-phase displacement vector. Each spring is accompanied by a damper representing the viscous fluid. Therefore, the equation of motion for the solid-phase displacement can be interpreted as a coupled spring-mass-damper system. A coupled system of only springs introduces collective vibrational modes such as those seen in lattice atomic vibrations. When dampers are added to the coupled springs, it is possible that the entire coupled system can be seen as an isolated spring-mass-damper system, but this depends on the excitation strength (Hollweg, 1997). Further analysis is required to interpret our simulation results in terms of the coupled spring-mass-damper system. More specifically, we aim to answer why the resonance peaks occur at 25 and 48 Hz. Hollweg (1997) states that it is possible for a system of coupled oscillators to behave like a single damped oscillator under certain conditions.

The resonance effect in our simulation is not caused by boundary conditions (simulation size) used. We have reduced the force peak magnitude from 10^7 N/m^2 to only 100 N/m^2, a five order of magnitude reduction, and find that the spatial patterns of u_z are unchanged. We note that u_z at the top surface determines the work-done spectrum (Fig. 4) since the force distribution is identical for all frequencies. Figure 7 shows the plot of u_z at 24 Hz on the surface for the two force peak values. The surface patterns are identical for the two force peaks. We conclude that this resonance effect is inherent in the governing equations.

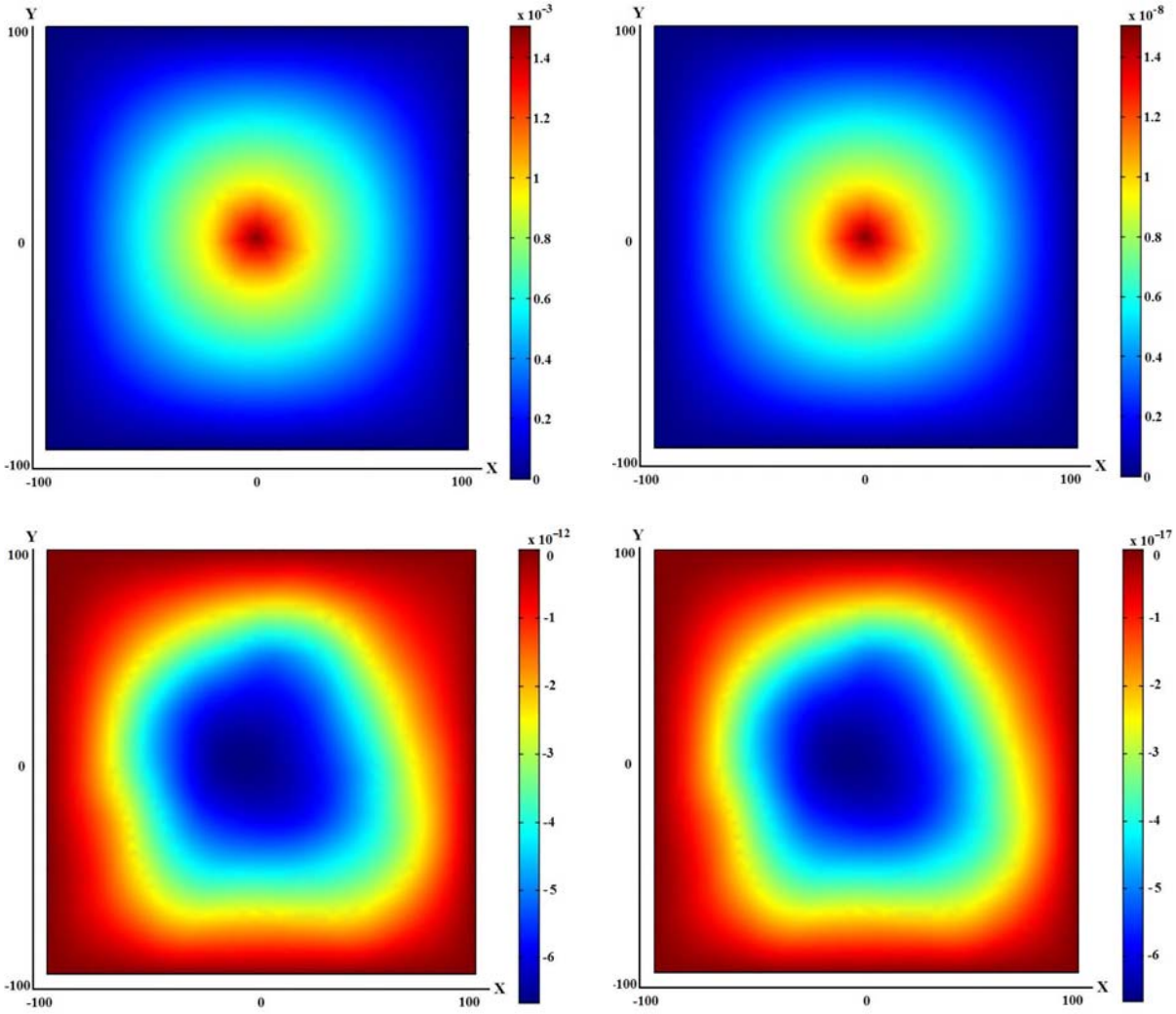

FIG. 7. The patterns shown by u_z at 24 Hz on the surface (z = 0) are independent of the force peak magnitude. The unit of u_z is meter. The real components of u_z for (a) the 10^7 and (b) the 100 N/m^2 peaks have the same spatial patterns (although of course their magnitudes are rescaled accordingly). The imaginary components of u_z for (c) the 10^7 and (d) the 100 N/m^2 peaks have also the same spatial patterns.

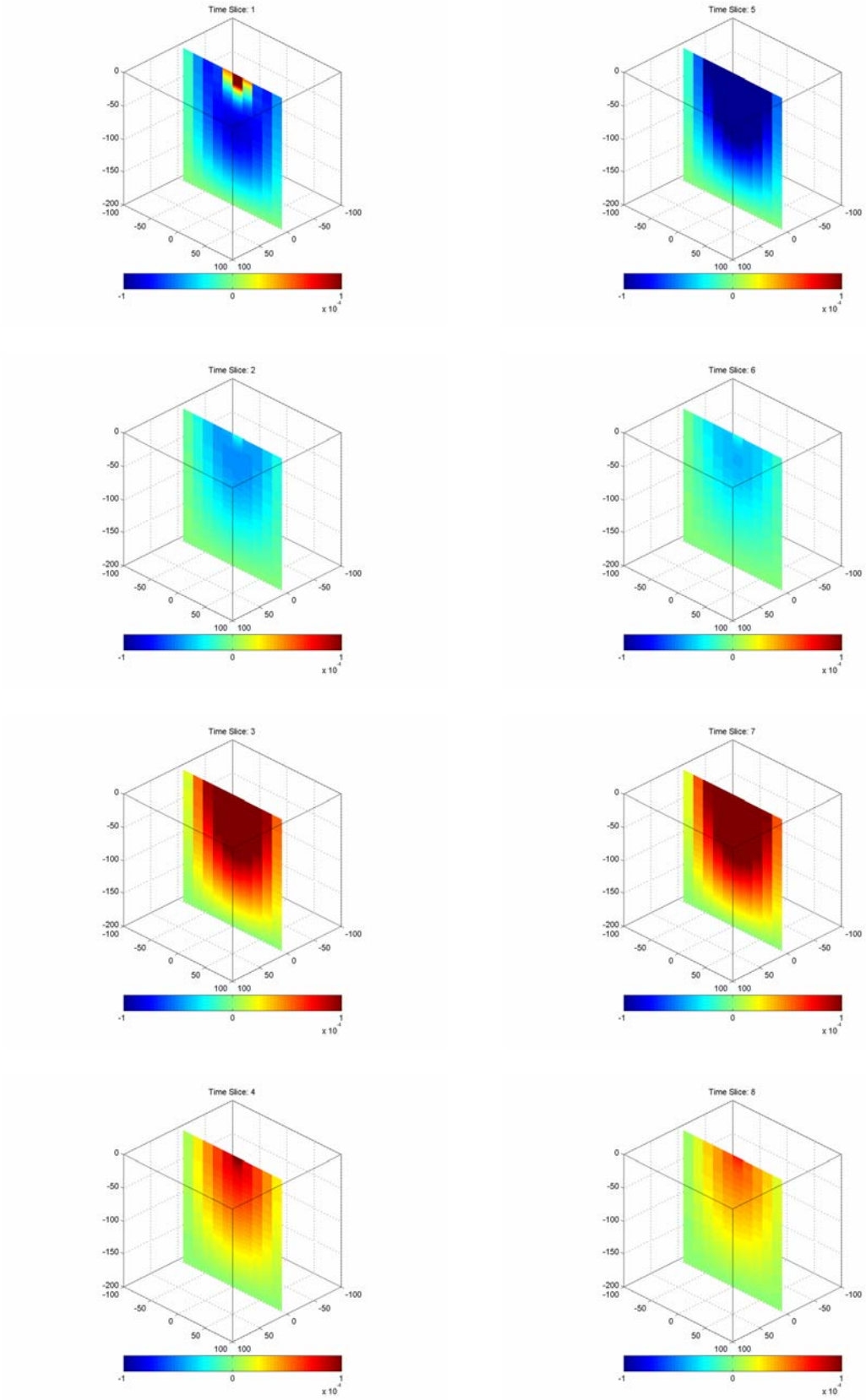

FIG. 8. Snapshots of solid phase displacement in the *z*-direction.

We$_z$ also perform a fast inverse Fourier transform to our frequency results (spanning from 1 to 32 Hz) to yield a time-dependent elastic displacement vector. While the frequency-domain results are useful for physical interpretations, the time-dependent elastic wave propagation results are useful for seismic interpretations. Figure 8 contains the results for u_z from the fast Fourier transform. The temporal progression starts at the top left (Time Slice 1) and ends at the bottom right (Time Slice 8) with a time interval of 31.25 ms. We use a narrow frequency band due to mainly very large computation time required. The elastic wave at the surface oscillates in time as expected and the wave decays to zero at the boundaries due to the Dirichlet conditions imposed.

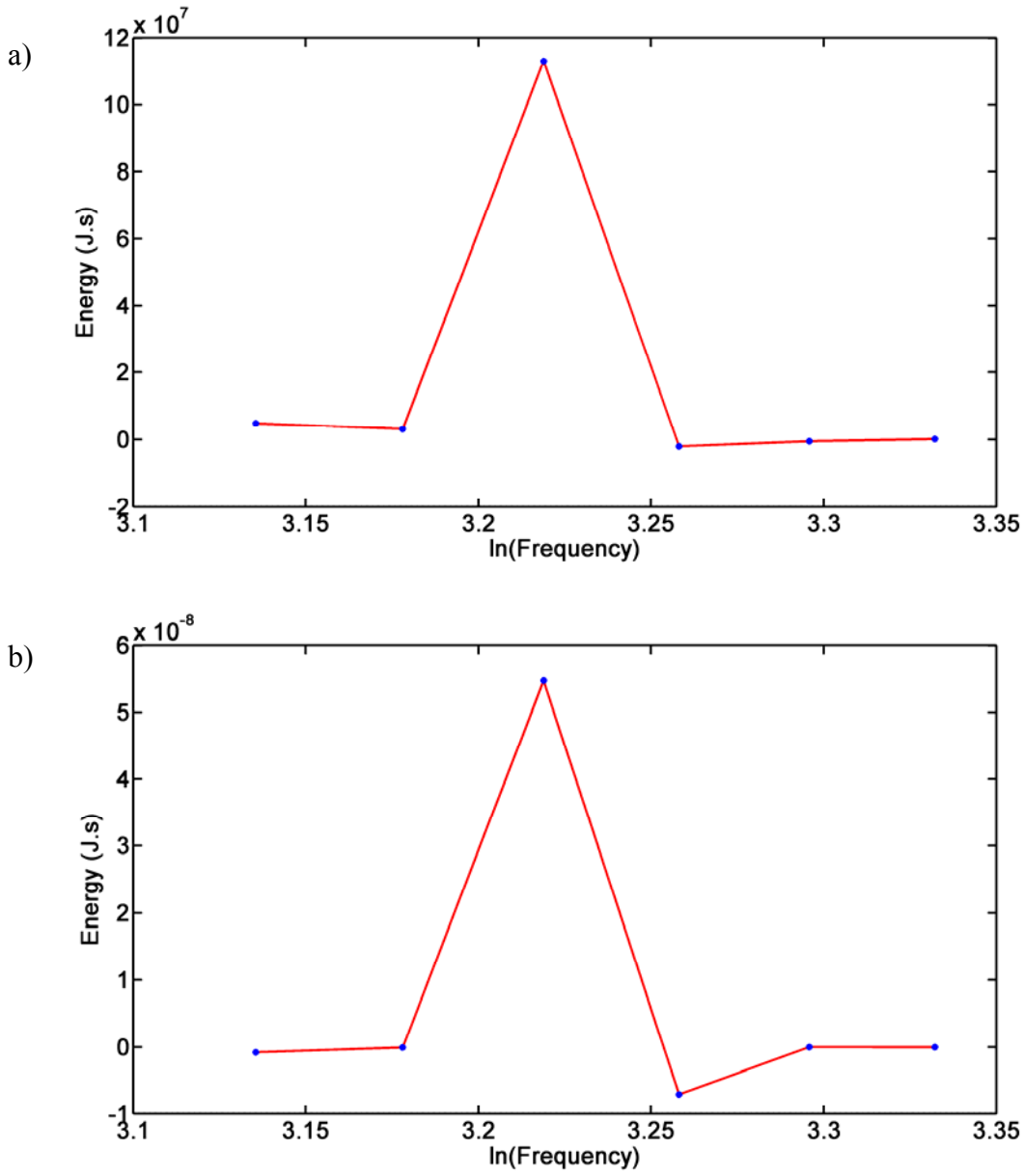

FIG. 9. (a) Real and (b) imaginary component of the elastic energy in the solid phase. We plot only data near the 25 Hz peak.

To probe further the resonance effect we propose, we perform simulations with fluid phase having a viscosity of 10^7 Pa·s and find the 25 Hz to broaden as displayed in Fig. 9(a)-(b). The peak remains at 25 Hz and the peak width does not increase significantly with the increased viscosity. The peak location in frequency is consistent with the absorption peak of the single damped oscillator model described earlier, where the resonance peak is not altered by increased viscous dissipation. However, the absence of broadening with increased viscosity is not consistent with the single damped oscillator model. Further analysis in comparing our results with a model of coupled damped oscillators is required.

The plot of $E_z(0,0,z)$, i.e., the z-component of the electric field vector at $(x,y) = (0,0)$ as a function of depth z, generated by the relative motion of opposite charged ions at the fluid-solid interface is displayed in Fig. 10. Boundary conditions are of Dirichlet type at the top surface ($z = 0$) and the bottom surface ($z = 200$). The magnitude increases rapidly between 24 and 32 Hz, corresponding to the increased energy absorption in the solid and fluid phases. The oscillation shows that electrical dipoles along the z-direction are realized. The real and imaginary components of the electric field are comparable and should be detectible in field experiments by installing voltage probes at two different depths. Such measurement techniques require boreholes. The low-frequency electric field corresponds to a diffusive process of ionic transport and we expect the electric field at this frequency band to produce essentially an Ohmic character of electrical conduction.

a)

b)

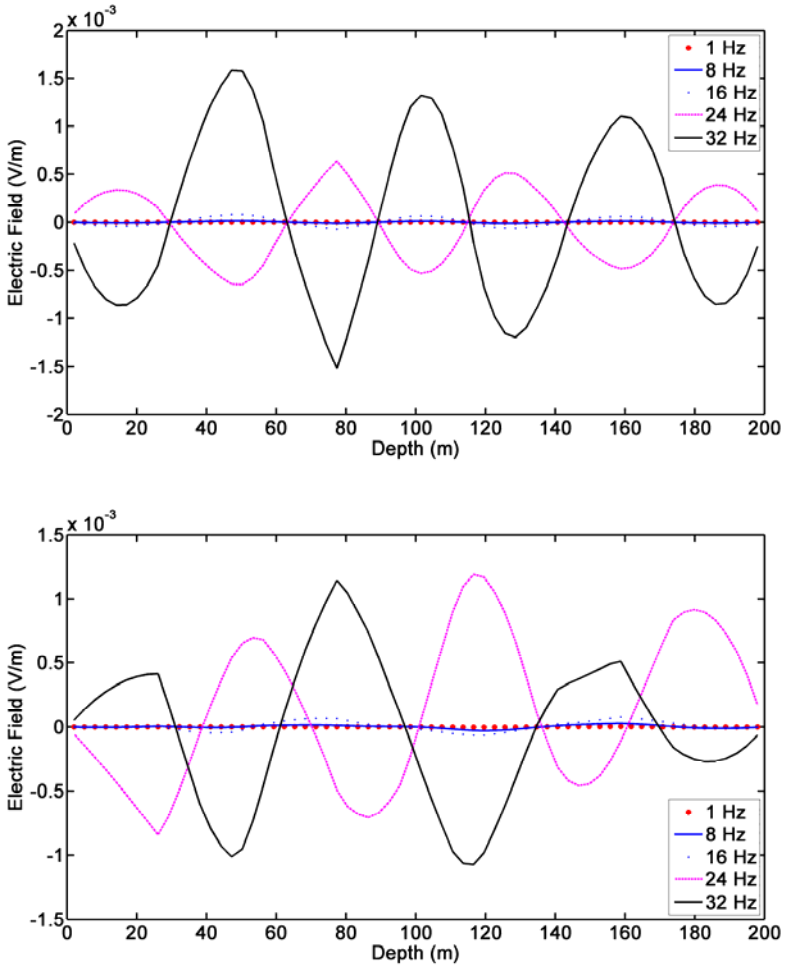

FIG. 10. (a) Real and (b) imaginary components of electric field in *z*-direction for frequency 1-32 Hz.

The electric fields in the *x*- and *y*-directions do not produce large-scale electrical dipoles. The randomly oriented dipoles at 16 and 24 Hz will make voltage measurements difficult to be performed in the field. The random patterns persist in most frequencies we tested. The seemingly chaotic patterns we believe are caused by the diffusive nature of the electrical conduction at low frequencies, although they are partially caused by the mesh geometries. We plan to perform simulations at higher frequencies (up to 1000 Hz) to see whether large-scale dipoles can be induced.

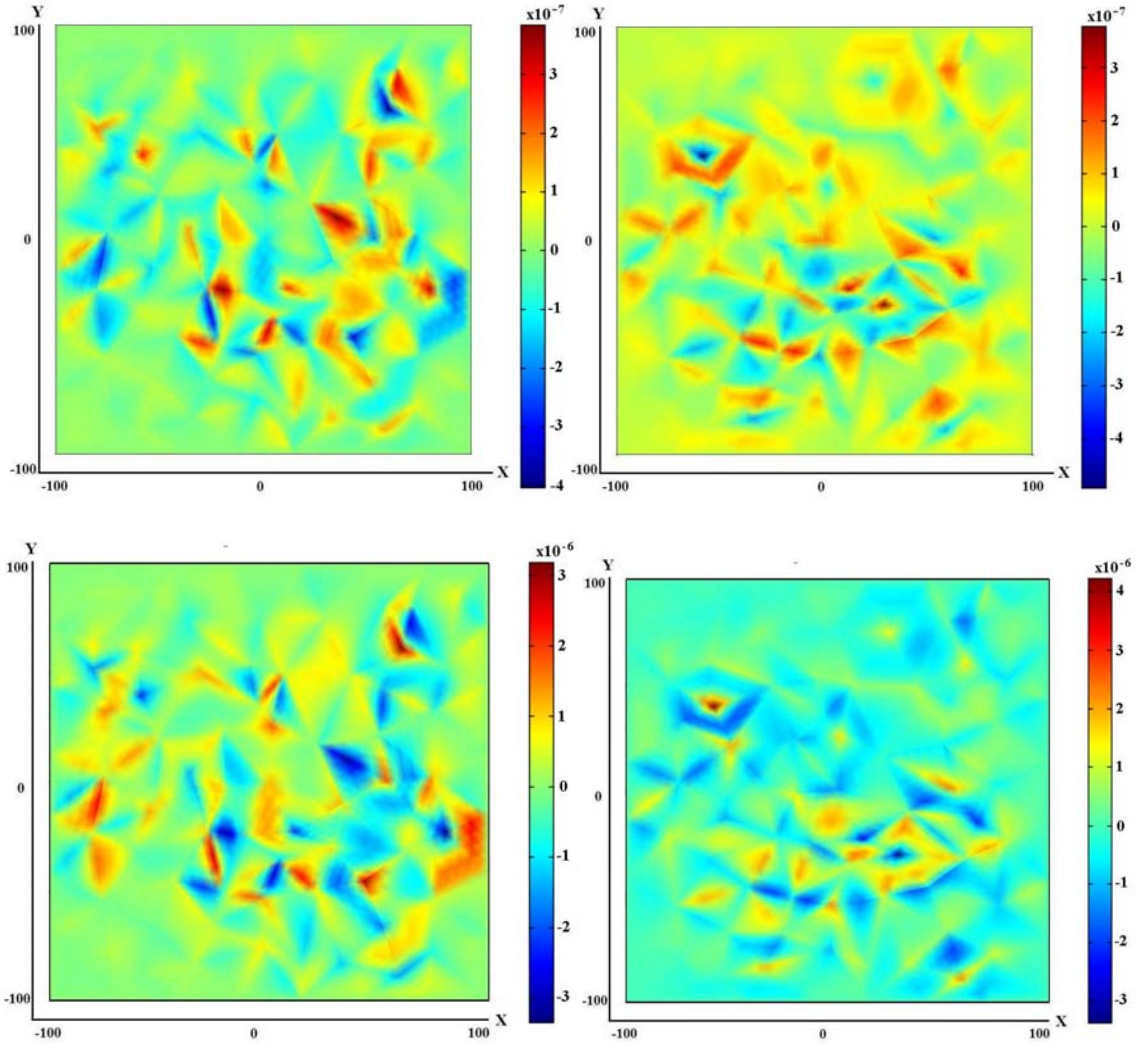

FIG. 11. The electric field produced at (top) 16 Hz and (bottom) 24 Hz. The left panels show the *x*-components, while the right panels show the *y*-components.

The magnetic field along the *z*-direction can generate a Lorentz force for an electrical current running along the *x*- and *y*-directions. This force will deflect the current direction toward the *y*- and *x*-directions, respectively. A Hall effect measurement may be able to detect this magnetic field generated by the induced electromagnetic field. Figure 12 plots the *z*-component of the magnetic field **B** on the surface at 16 and 24 Hz. Its magnitude is around 1 nT. The strength of stray magnetic field from the Earth can range from 0 to 300 nT (Hand, 1976). We believe our simulation results have demonstrated a promising opportunity to detect the seismoelectric signal using the Hall effect. What is important is appropriate frequency isolation from the stray field.

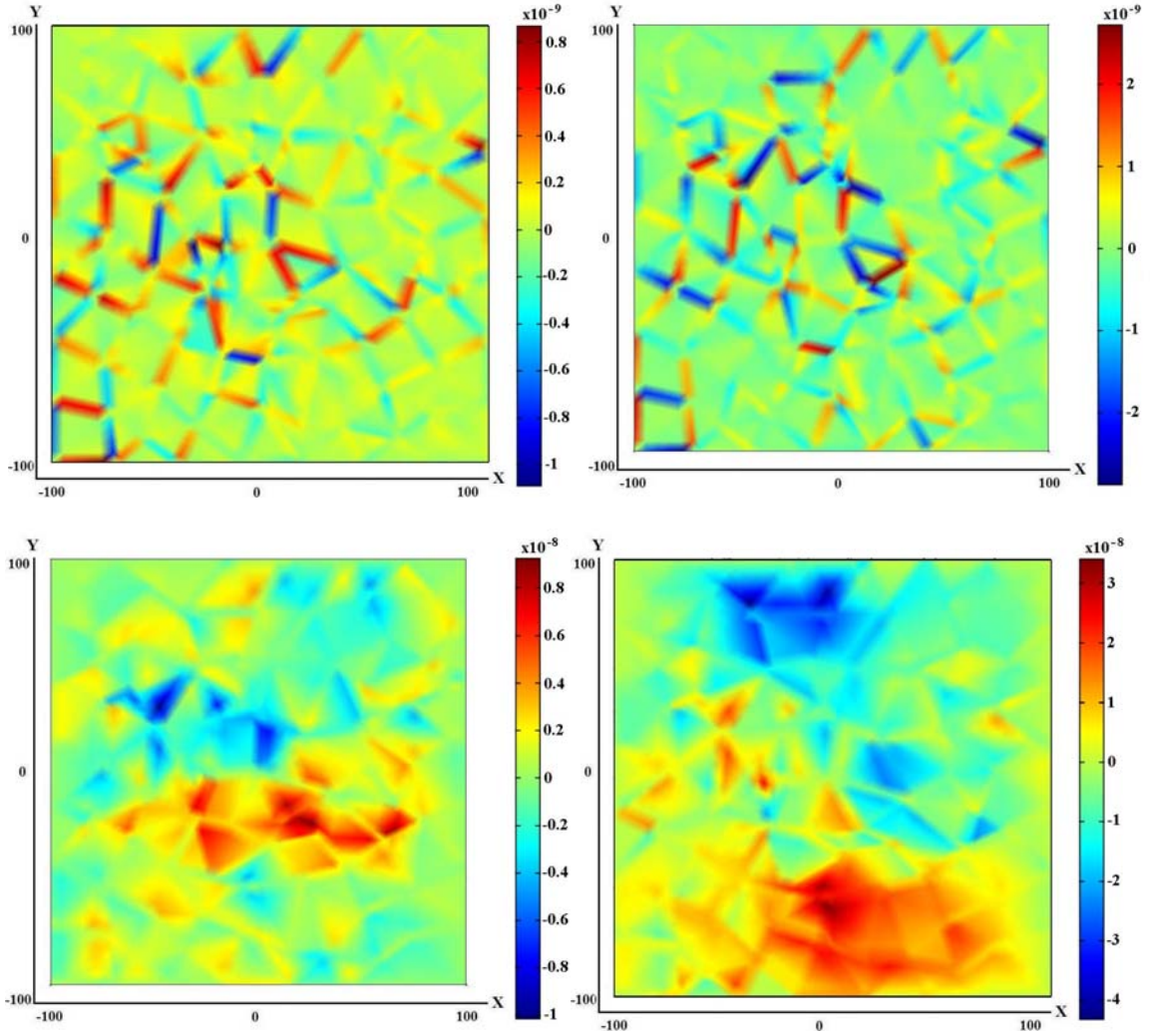

FIG. 12. Top panels show magnetic field along the *z*-direction on the surface (z = 0) at (left) 16 Hz and (right) 24 Hz. The bottom panels are the magnetic field along the *x*-direction on the surface at (left) 16 Hz and (right) 24 Hz.

CONCLUSIONS

We have numerically demonstrated that the frequency response of a homogeneous and saturated porous soil possesses a resonance behaviour at two distinct frequencies. A sharp peak at around 25 Hz is attributed to the elastic resonance of the soil, while the peak at around 48 Hz is broader and the broadening may be caused by viscous drag force from the fluid phase. The energy analysis finds that almost the entire work done by the surface force excitation from the single-shot explosion is stored as elastic energy in the solid phase. The resonance peaks in the fluid and the solid phases coincide, which suggest they behave synchronously within the frequency range of 0-64 Hz. This result alone convinces us that more significant seismoelectric signal generation can be obtained at higher frequencies, where relative motion between the fluid and solid phases becomes more pronounced. We suspect the Biot fluid energy expression does not incorporate the contribution from fluid pressure. Theoretical investigation into the governing equations should give us additional insight into the resonance effect observed in our simulations.

magnitude of induced magnetic field is around 1-10 nT, and we believe it should detectible using high-precision magnetometers, such those based on Hall effect.

ACKNOWLEDGEMENTS

The work of Seismoelectric simulation was supported by AERI (Alberta Energy Research Institute) Project #1571. We would also like to thank CREWES for technical support.

REFERENCES

Buttler, K.E., Russel R.D., Kepic A.W. and Maxwell M., 1996, Measurements of the seismoelectric response from a shallow boundary, Geophysics, **61**, 1769-1778.

Block, G. I. and Harris J.G., 2006, Conductivity dependence of seismoelectric wave phenomena in fluid-saturated sediments, J. Geophys. Res., **111**, 1-12.

Chen, Benchi and Mu Y., 2005, Experimental studies of seismoelectric effects in fluid-saturated porous media, J. of Geophys and Eng., **2**, 222-230.

Garambois, S. and Dietrich M., 2002, Full waveform numerical simulation of seismoelctromagnetic wave conversions in fluid-saturated stratified porous media, J. Geophys. Res., **107**, 1-17.

Garambois, S. and Dietrich M., 2001, Seismoelectric wave conversions in porous media: Field measurement and transfer function analysis, Geophysics, **66**, 1417-1430.

Hall, J. W., 1976, A servo system for reducing stray AC magnetic fields in an iron-free environment, J. Phys. E: Scientific Instruments, **9**, 920.

Hollweg, J. V., 1997, A simple mechanical model for resonance absorption: The Alfven resonance, J. Geophys. Res. **102**, 24127.

Landau, L. D. and Lifshitz, E. M., 1995, Theory of Elasticity (Butterworth-Heinemann, Oxford), pp. 22-25.

Pride, S.R., 1994, Governing Equations for the coupled electromagnetics and acoustics of porous media, Phys. Rev. B, **50**, 15,678-15,696.

Thompson, A.H., and Gist G.A., 1993, Geophysical applications of electrokinetic conversion, Leading Edge, **12**, 1169-1173.